

# Initial physics achievements of large helical device experiments

言語: eng

出版者:

公開日: 2009-02-24

キーワード (Ja):

キーワード (En):

作成者: Motojima, O., Yamada, H., Komori, A., Ohyabu, N., Kawahata, K., Kaneko, O., Masuzaki, S., Ejiri, A., Emoto, M., Funaba, H., Goto, M., Ida, K., Idei, H., Inagaki, S., Inoue, N., Kado, S., Kubo, S., Kumazawa, R., Minami, T., Miyazawa, J., Morisaki, T., Morita, S., Murakami, S., Muto, S., Mutoh, T., Nagayama, Y., Nakamura, Y., Nakanishi, H., Narihara, K., Nishimura, K., Noda, N., Kobuchi, T., Ohdachi, S., Oka, Y., Osakabe, M., Ozaki, T., Peterson, B.J., Sagara, A., Sakakibara, S., Sakamoto, R., Sasao, H., Sasao, M., Sato, K., Sato, M., Seki, T., Shimosuma, T., Shoji, M., Suzuki, H., Takeiri, Y., Tanaka, K., Toi, K., Tokuzawa, T., Tsumori, K., Tsuzuki, K., Yamada, I., Yamaguchi, S., Yokoyama, M., Watanabe, K.Y., Watari, T., Hamada, Y., Matsuoka, K., Murai, K., Ohkubo, K., Ohtake, I., Okamoto, M., Satoh, S., Satow, T., Sudo, S., Tanahashi, S., Yamazaki, K., Fujiwara, M., Iiyoshi, A.

メールアドレス:

# Initial physics achievements of large helical device experiments\*

O. Motojima,<sup>†a)</sup> H. Yamada, A. Komori, N. Ohyabu, K. Kawahata, O. Kaneko, S. Masuzaki, A. Ejiri, M. Emoto, H. Funaba, M. Goto, K. Ida, H. Idei, S. Inagaki, N. Inoue, S. Kado, S. Kubo, R. Kumazawa, T. Minami, J. Miyazawa, T. Morisaki, S. Morita, S. Murakami, S. Muto, T. Mutoh, Y. Nagayama, Y. Nakamura, H. Nakanishi, K. Narihara, K. Nishimura, N. Noda, T. Kobuchi, S. Ohdachi, Y. Oka, M. Osakabe, T. Ozaki, B. J. Peterson, A. Sagara, S. Sakakibara, R. Sakamoto, H. Sasao, M. Sasao, K. Sato, M. Sato, T. Seki, T. Shimoizuma, M. Shoji, H. Suzuki, Y. Takeiri, K. Tanaka, K. Toi, T. Tokuzawa, K. Tsumori, K. Tsuzuki, I. Yamada, S. Yamaguchi, M. Yokoyama, K. Y. Watanabe, T. Watari, Y. Hamada, K. Matsuoka, K. Murai, K. Ohkubo, I. Ohtake, M. Okamoto, S. Satoh, T. Satow, S. Sudo, S. Tanahashi, K. Yamazaki, M. Fujiwara, and A. Iiyoshi

*National Institute for Fusion Science, Oroshi-cho, Toki-shi, Gifu 507-8292, Japan*

(Received 16 November 1998; accepted 8 December 1998)

The Large Helical Device (LHD) experiments [O. Motojima, *et al.*, Proceedings, 16th Conference on Fusion Energy, Montreal, 1996 (International Atomic Energy Agency, Vienna, 1997), Vol. 3, p. 437] have started this year after a successful eight-year construction and test period of the fully superconducting facility. LHD investigates a variety of physics issues on large scale heliotron plasmas ( $R=3.9$  m,  $a=0.6$  m), which stimulates efforts to explore currentless and disruption-free steady plasmas under an optimized configuration. A magnetic field mapping has demonstrated the nested and healthy structure of magnetic surfaces, which indicates the successful completion of the physical design and the effectiveness of engineering quality control during the fabrication. Heating by 3 MW of neutral beam injection (NBI) has produced plasmas with a fusion triple product of  $8 \times 10^{18}$  keV m<sup>-3</sup> s at a magnetic field of 1.5 T. An electron temperature of 1.5 keV and an ion temperature of 1.4 keV have been achieved. The maximum stored energy has reached 0.22 MJ, which corresponds to  $\langle \beta \rangle = 0.7\%$ , with neither unexpected confinement deterioration nor visible magnetohydrodynamics (MHD) instabilities. Energy confinement times, reaching 0.17 s at the maximum, have shown a trend similar to the present scaling law derived from the existing medium sized helical devices, but enhanced by 50%. The knowledge on transport, MHD, divertor, and long pulse operation, etc., are now rapidly increasing, which implies the successful progress of physics experiments on helical currentless-toroidal plasmas. © 1999 American Institute of Physics. [S1070-664X(99)90605-5]

## I. INTRODUCTION

The Large Helical Device (LHD) is a large-scale superconducting toroidal fusion facility, which is a heliotron type device with a set of  $l=2/m=10$  continuous helical coils.<sup>1,2</sup> The major and minor radii are 3.9 m and 0.6 m, respectively. LHD has the capability of steady-state operation by means of superconducting coils in addition to the physical intrinsic potential of the heliotron configuration, which is free from current drive and disruption. A built-in helical divertor with a double-null structure provides the necessary edge heat and particle control for steady-state plasma sustainment as well as confinement improvement. The advanced currentless experiments in LHD emphasize the following objectives: (1) to achieve high-performance steady-state plasmas extrapolatable to reactor conditions; (2) to explore the existing physical issues in toroidal plasmas; and (3) to develop necessary issues on fusion technology. This article describes the physical

findings in the initial experiments which have widened the operational regime significantly from the existing helical devices. Understanding of currentless plasmas has progressed in the medium-sized helical devices [Compact Helical System (CHS), Heliotron E, Wendelstein VII-AS, and Advanced Toroidal Facility].<sup>3</sup> Basic performance of confinement in helical devices is comparable to low(L)-mode plasmas in tokamaks with similar dimensions. Clear evidence of further confinement improvement has also been observed.<sup>4-6</sup> However, the enhancement factor of confinement has been smaller than in large tokamaks. The reasons can be attributed to connection of the boundary where neutrals and atomic processes play an essential role and the core where high-temperature plasmas are contained. LHD has enough size to possibly exclude such complicated conditions. The neoclassical transport properties becomes more evident in the radial transport in large-scale helical systems.

LHD has three pairs of poloidal coils which provide three degrees of freedom in the magnetic field, i.e., the dipole, quadrupole fields, and the leakage poloidal flux. They can be used to control the radial position, elongation, and

\*Paper J5I1.2 Bull. Am. Phys. Soc. **43**, 1776 (1998).

<sup>†</sup>Invited speaker.

<sup>a)</sup>Electronic mail: motojima@lhd.nifs.ac.jp

loop voltage. The magnetic geometry in this study is set at the optimized one from MHD stability in terms of ideal interchange modes, neoclassical transport, and particle confinement, in particular, fast ion loss. The magnetic axis is set at 3.75 m which is shifted inward from the machine center and the averaged elongation is 1. In this configuration, the mod-B surfaces do not deviate from flux surfaces so much that confinement property of trapped particles is improved. Although the inward-shifted configuration has a magnetic hill, spontaneous generation of a magnetic well due to the Shafranov shift stabilizes interchange modes in the core region. The strong magnetic shear instead of a magnetic well stabilizes these modes in the edge region. The magnetic field has been limited to 1.5 T in the plasma experiments for the sake of compilation of operational experience of large-scale superconducting coils. The magnetic field alone indeed has already reached 2.7 T in the engineering operation. The present surface of the plasma vacuum vessel is bare stainless steel and has been conditioned by discharge cleaning of helium glow or electron cyclotron resonance (ECR) (2.45-GHz) direct current (dc) plasmas, and by titanium gettering with a coverage area of 20%. Divertor plates other than a model plate which works as a probe station have not been installed. Second harmonic 84-GHz electron cyclotron heating (ECH) up to 400 kW has been employed to generate plasmas, which are targets for NBI. Two negative-ion-based neutral beam injectors are aligned for tangential injection in opposing directions, i.e., co- and counter-injection to cancel out beam driven toroidal currents. Each injector is designed to inject 7.5-MW hydrogen beams at an energy of 180 keV for 10 s. In the initial experiments, the ion sources are optimized for a lower energy up to 100 keV considering compatibility with the low-density target plasmas at 1.5 T operation. Therefore the available beam injection power is 3-MW total in this study. A variety of diagnostics that enable profile measurements is available, such as YAG-laser Thomson scattering for the electron temperature, charge-exchange-recombination spectroscopy (CXRS) for the ion temperature, multi-chord far-infrared (FIR) interferometer for the electron density, a soft X-ray array, a bolometer array, and a Langmuir probe array on the model divertor plate.

## II. FIELD MAPPING

In helical systems, it is required and possible to demonstrate the existence of well-nested vacuum magnetic surfaces by an electron beam mapping method. In parallel with the high-temperature plasma experiment, the magnetic surface mapping has been done to clarify completeness of both physical design and fabrication, which gives a fundamental basis to the confinement studies. A LaB<sub>6</sub> cathode which works under the strong magnetic field as high as 4 T generates an electron beam with a diameter of 3 mm and an acceleration voltage of up to 200 V. The mesh applied ZnO(P-15) with a transparency of 83% is set on a vertically elongated cross-section and covers the entire magnetic surfaces. The pictures were taken by an intensified charge coupled device (CCD) camera with a tangential view. Although the mapping can be done in the full magnetic field to

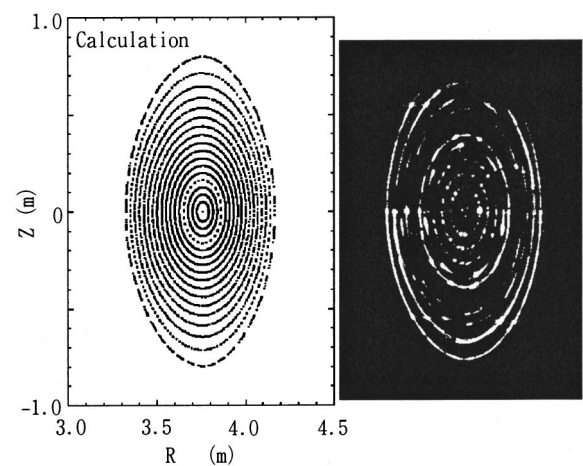


FIG. 1. Mapping of magnetic surfaces of the standard configuration of LHD. Left hand side: Calculation in the vacuum magnetic field. Right hand side: Experimental measurement by the electron beam and the fluorescent mesh. The magnetic field strength is 0.25 T.

take advantage of the superconducting coils, the experimental field was limited to 0.25 T because the radial scan of the electron gun to sweep the magnetic surfaces had to be operated manually for the initial measurement. The vacuum condition is on the order of  $1 \times 10^{-6}$  Pa and generation of plasma by electron beams degrades the quality of the mapping measurement above that vacuum level.

Figure 1 shows the predicted and measured flux surfaces. It is clear that the structure of nested flux surfaces agrees with each other, which demonstrates the accuracy of the superconducting coils. The scan of poloidal fields to shift the surfaces in major radius also shows remarkable agreement between experiments and calculations. Since the present magnetic field is low, the effect of terrestrial magnetism is visible. The  $m = 1/n = 1$  island observed in the periphery is consistent with the resonance with the terrestrial magnetic field in both phase and size. Also, rotational transform evaluated from the transit map agrees with the calculation.

## III. DISCHARGE CHARACTERISTICS OF CURRENTLESS PLASMAS

The first experimental campaign was focused on the start-up of ECH with limited available resources and ended successfully in the middle of May 1998. The second experimental campaign has started in the middle of September 1998 after two-months of work in the vented vacuum vessel. Baking at a temperature of 95 °C and He glow discharge cleaning have evacuated oxygen and carbon impurities equivalent to 90 mono-layers from the surface of the vacuum vessel before the start of the second experimental campaign. Then the NBI experiments were started successfully. The alternating of high-temperature plasma discharges and helium dc discharges by glow or 2.45-GHz ECR is effective for wall conditioning. Progress in wall conditioning and increase of available heating power enable remarkable steady progress of plasma performance (see Fig. 2). Titanium gettering has also contributed to the rapid and efficient conditioning in the initial phase, which covers about 20% of the

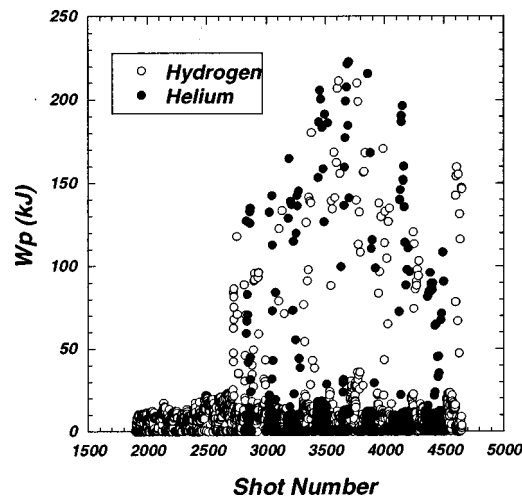


FIG. 2. Progress in the plasma performance. The obtained stored energy as a function of the shot number. Open circles: Hydrogen plasmas. Closed circles: Helium plasmas. NBI has started from the shot number 2722.

surface area of the plasma vacuum chamber. NBI plasmas are highlighted in this paper since ECH has been devoted to generate the target plasmas for NBI.

The ECH power of up to 450 kW is applied to produce target plasmas with a density of more than  $1 \times 10^{19} \text{ m}^{-3}$  so as to limit the shine-through of NBI to less than 40%. Since the density is crucial for the NBI target, the temperature in the ECH phase is limited to around 500 eV. Then NBI up to 3 MW is injected. The plasma density is controlled by gas-puffing, however, the density clamping with a rapid pump-out has been observed in hydrogen discharges. This phenomenon has been much mitigated in helium discharges.

Waveforms of a typical hydrogen discharge are shown in Fig. 3(a). Since the target ECH plasmas are well fueled, the plasmas are thin and detached. The plasma expands in the radial direction with increasing temperature and density due to NBI. When the high-temperature plasma reaches the magnetic boundary, a divertor channel is formed. The events of rapid pump-out of density, a decrease of radiation, and bursts of divertor flux begin at this time. The decay time of the decrease in density is enhanced by an increase of the heating power. Density does not build up efficiently despite strong gas puffing in the pump-out phase for several hundreds of ms. The decrease in total radiation and emission of light impurity lines are attributed to a rapid increase of edge temperature. This phenomenon is described in detail in the next section. The pump-out phenomenon is much milder in helium discharges and density can be maintained by recycling instead of auxiliary gas puffing since the metallic wall does not pump helium [see Fig. 3(b)]. Helium plasmas also mitigate the shine-through losses of NBI in the low-density regime. In a hydrogen discharge, a broad density profile becomes hollow when the pump-out starts. A broad density profile is maintained throughout a helium discharge and the edge density is higher than that in a hydrogen discharge, which is due to a larger neutral source from recycling. The temperature profile is more peaked in a hydrogen discharge than a helium one.

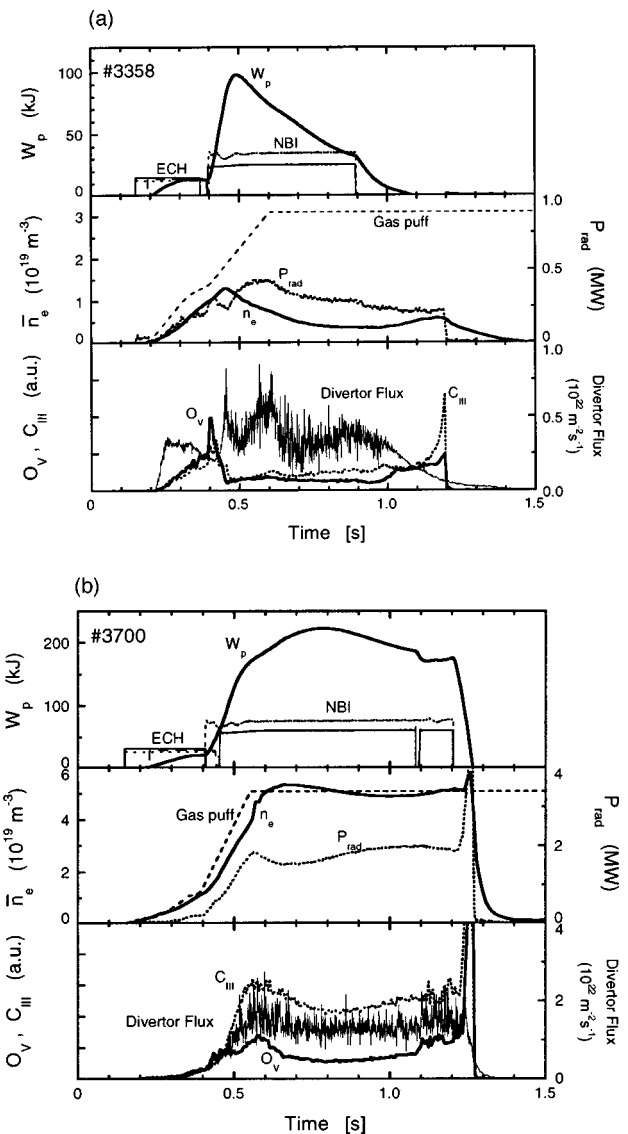


FIG. 3. Temporal behavior of typical NBI heated plasmas in the initial experiments. (a) Hydrogen discharge. (b) Helium discharge. Stored energy is measured by the diamagnetic loop. Dotted lines illustrated with density are the predicted densities assuming 100% efficiency of fueling.

The present operational density limits bounded by radiation collapses are  $4.5 \times 10^{19} \text{ m}^{-3}$  in hydrogen plasmas with a gas puff,  $6.0 \times 10^{19} \text{ m}^{-3}$  in hydrogen plasmas with pellet injection, and  $6.3 \times 10^{19} \text{ m}^{-3}$  for helium plasmas (see Fig. 4). The radiation collapse phenomena can be classified into two types. The first type is characterized by a hollow radiation profile that increases symmetrically until the radiation collapse. In these instances the total radiated power is at or below the beam input power. In these discharges the stored energy drops steadily to zero on a time scale of around 100 ms. The second type is characterized by a rapid increase in the total radiated power over a 100-ms time scale resulting in an instantaneous peak radiated power, which is larger than the input heating power. The radiation profile shows a sharp peaking on the inboard side of the plasma which increases and moves toward the center of the plasma in 30 ms.

Hollow density profiles have been frequently observed in helical devices, in particular, with ECH. A neoclassical

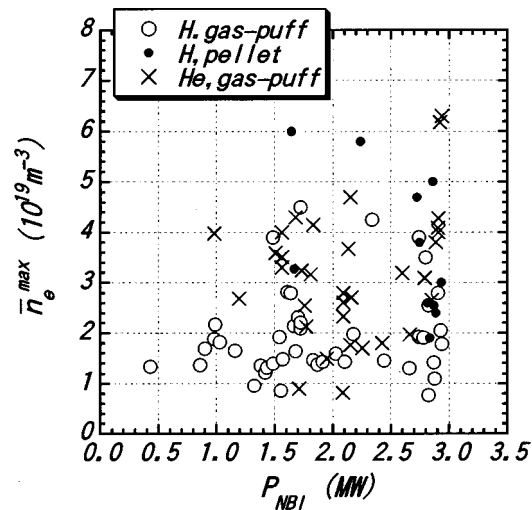


FIG. 4. Operational regime in density and heating power of NBI in hydrogen discharges with gas-puffing (open circles) and pellet injection (closed circles) and helium discharges with gas-puffing (crosses).

theory<sup>7</sup> has pointed out that the off-diagonal term of the temperature gradient enhances particle flux and leads to hollow density. This problem may be pronounced more in large-scale plasmas. The poloidal rotation which is closely connected to the radial electric field  $E_r$ , has been measured by CXRS. A change in the direction of the rotation has been observed before and after the start of pump-out in a hydrogen discharge. The plasma rotates initially in the electron diamagnetic direction and then changes to the ion diamagnetic direction. This may reflect a change in the sign of  $E_r$  from negative to positive, which is similar to the experimental results in CHS.<sup>8</sup>

Figure 5 shows a typical discharge with pellet injection. The size and the speed of the pellet are 3 mm diameter and 1 km/s, respectively. The pellet is broken into small pieces intentionally to avoid deep penetration in this case. A pellet is effective in increasing the density and as well as the stored

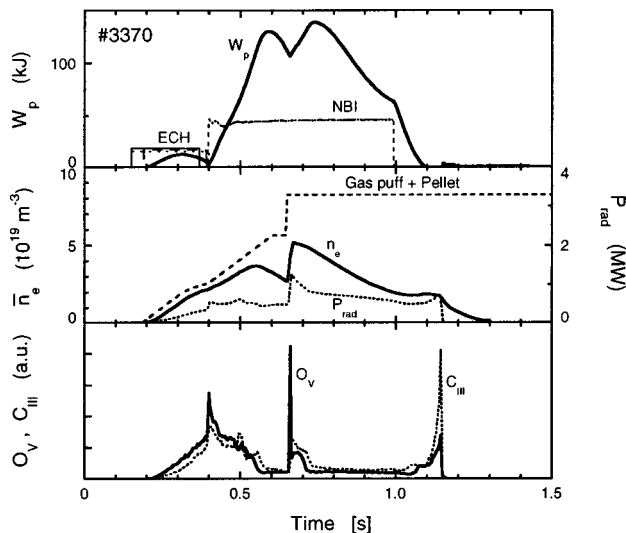


FIG. 5. Temporal behavior in a pellet injected discharge. The pellet is injected at 0.655 s.

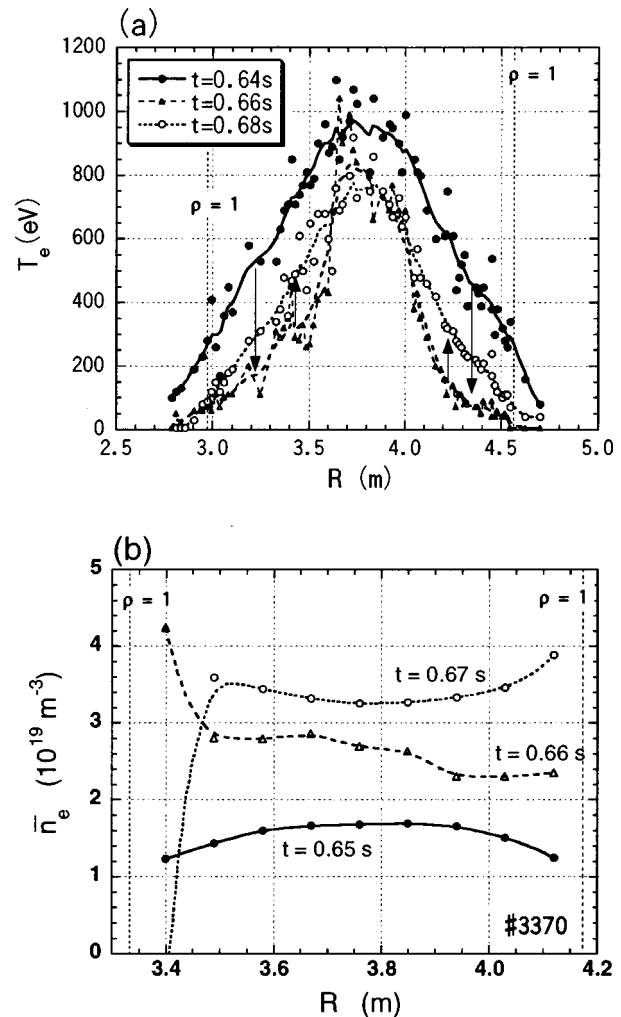


FIG. 6. Profile changes due to pellet injection in the discharge shown in Fig. 5. (a) Electron temperature profile along the major radius measured by YAG Thomson scattering system. Measured points are scanned horizontally on the oblate cross section.  $\rho=1$  denotes the position of the last closed flux surface. (b) Line averaged electron density. Measured chords are vertical in the prolate cross section.

energy. The change of plasma profile is shown in Fig. 6. An abrupt decrease of temperature is observed in the peripheral region and the temperature comes back in a very short time scale. However, the central temperature certainly drops suddenly and continues to decrease slowly and comes back in the time scale of an energy confinement time. The density increase is also observed in the peripheral region. These observations in temperature and density suggest that the pellet ablates in the intermediate region and does not penetrate to the center. This agrees with the prediction from the pellet ablation model. In this case, the pellet injection does not give rise to a peaked density profile although the trigger of inward pinch has been observed in other devices.<sup>6</sup> The decay time of the density after the pellet injection is the same as that before the injection, which may be consistent with the absence of an inward pinch. A full solid pellet penetrates to the center and forms a peaked density profile. However, the density profile flattens again after pellet injection and consequently becomes hollow after a few hundreds of ms.

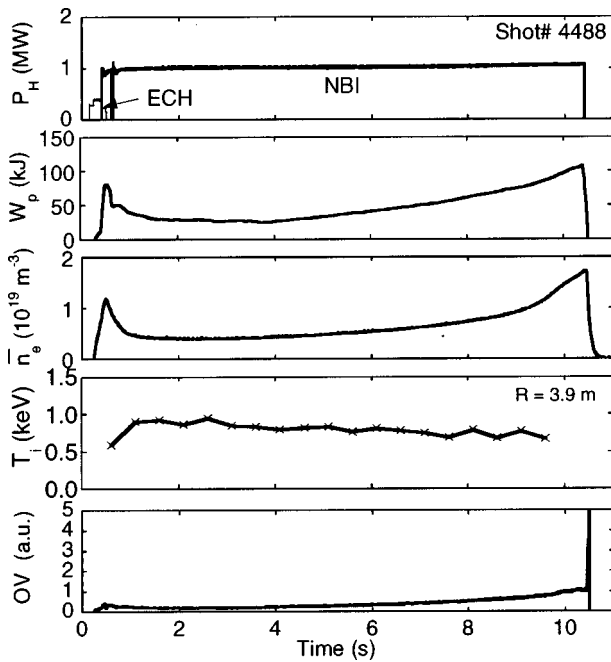


FIG. 7. Long-pulse NBI discharge with helium gas. Ion temperature is measured by CXRS.

By making use of stable recycling in helium, a long pulse operation is obtained. Figure 7 shows the 10-s long discharge with NBI. The quasi-steady-state is achieved for several seconds. Density increase despite no gas-puffing terminates the plasma eventually, and the combination of efficient fueling and pumping is required for further longer discharges.

#### IV. CONFINEMENT STUDY

Energy confinement times are evaluated from the stored energy measured by diamagnetic loops. The response of diamagnetic loops has been calculated by the three-dimensional (3-D) magnetic field. The NBI power deposition is modeled by the database from a number of runs of a 3-D Monte Carlo simulation code for Neutral Beam Injection (MCNBI).<sup>9</sup> In heliotrons, the Shafranov shift due to finite- $\beta$  effects changes the beam birth profile and the drift orbit of beam particles. Therefore, in this code, the 3-D magnetic configuration including the finite- $\beta$  effect is used for the evaluation of the deposition profile. The computational results suggest that heating efficiency and deposition profiles are not different for the cases of co- and counter-injection in the current experimental condition. The stored energy derived from kinetic profile measurements agrees well with the diamagnetic measurement. This supports the validity of the NBI power deposition model which suggests a negligible effect of the beam pressure (at most of a few per cent).

Four major inter-machine scalings of energy confinement time for helical devices [LHD scaling,<sup>10</sup> Lackner-Gottardi (L-G) scaling,<sup>11</sup> gyro-reduced Bohm,<sup>12</sup> and International Stellarator Scaling 95 (ISS95)<sup>13</sup>] have been proposed so far and all describe similar trends of deterioration with power and apparent positive density dependences. The international stellarator scaling 95 (ISS95) expresses,

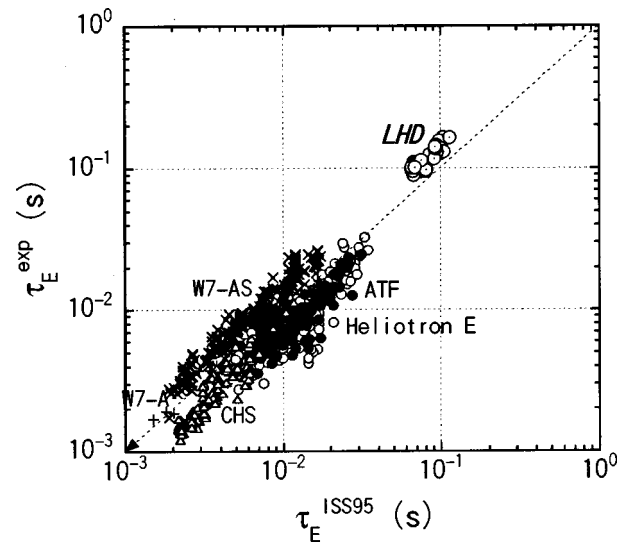


FIG. 8. Comparison of confinement times obtained in the experiments and prediction from the ISS95 expression. The medium sized existing helical experiments are also illustrated.

$$\tau_E = 0.079 a^{2.21} R^{0.65} P^{-0.59} \bar{n}_e^{0.51} B_t^{0.83} t_{2/3}^{0.4},$$

with  $\tau_E$  in s,  $a$  and  $R$  in m,  $P$  in MW,  $\bar{n}_e$  in  $10^{19} \text{ m}^{-3}$ , and  $B_t$  in T. While this scaling describes L-mode plasmas in large tokamaks as well, the density dependence is pronounced unlike in the tokamak L-mode scaling. From experience in tokamaks, larger devices which have less heating power density make the transition to saturation from linear ohmic confinement in the lower density regime, which is connected to an L-mode with auxiliary heating. This issue is crucial for the prospects of helical devices since the present reactor design relies on the favorable density dependence on confinement.

Figure 8 shows the comparison of experimental data with the prediction from the ISS95 expression. The achievements of LHD are larger than the presently existing helical devices by one order of magnitude. The density and absorbed power ranges cover  $1.0\text{--}5.0 \times 10^{19} \text{ m}^{-3}$  and  $0.5\text{--}2.3$  MW. The data in hydrogen discharges have been adopted here, since the estimate of power deposition in helium discharges cannot be discussed with the same accuracy as in hydrogen now. While the trend of energy confinement times of NBI heated plasmas in LHD is similar to ISS95, experimental data are systematically better than ISS95 by a factor of 1.5. Deviation from the scalings indicates an enhancement of a factor of 2 from the LHD scaling and is comparable to the L-G scaling.

In the current density range, the power deposition of NBI is a strong function of density. Deposition power increases by 50% with the density increase from  $2 \times 10^{19} \text{ m}^{-3}$  to  $4 \times 10^{19} \text{ m}^{-3}$  for the same port-through power. Since the data are not distributed sufficiently on the space of the density and the absorbed power, there exists a correlation between the density and the absorbed power. Therefore it is difficult to distinguish whether confinement saturation in the relatively high-density regime is attributed to power degradation or vanishing of a density dependence. However, there

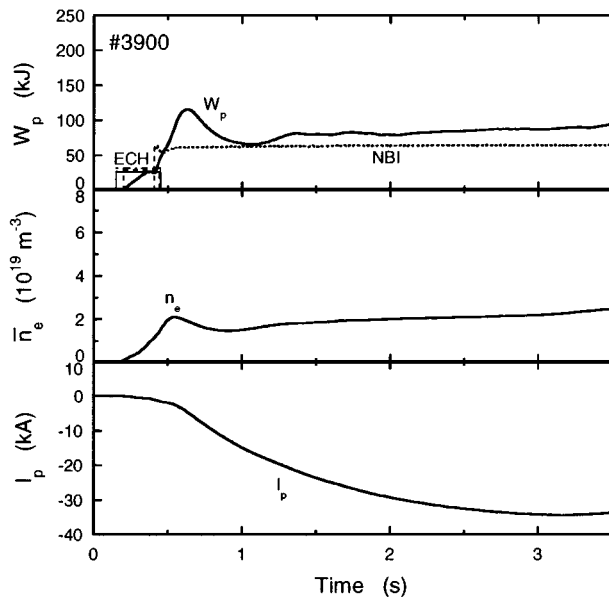


FIG. 9. Build-up of toroidal currents in a co-injected NBI discharge. The negative sign of the toroidal current defines the paramagnetic direction.

exist two sequences with the same deposition power and the different density. These are the discharges with 2 NBIs with  $1.5\text{--}1.8 \times 10^{19} \text{ m}^{-3}$  obtained by gas-puffing and the others are the discharges with 1 NBI with  $3 \times 10^{19} \text{ m}^{-3}$  times obtained by pellet injection. Comparison of these sequences indicates that energy confinement is improved with the square root of the density in the accessible density range ( $3 \times 10^{19} \text{ m}^{-3}$ ) with a power density of  $40 \text{ kW/m}^3$  although saturation of confinement is predicted to occur at  $1.7 \times 10^{19} \text{ m}^{-3}$  according to the tokamak experience of transition from the linear ohmic confinement to the saturated ohmic confinement. However, further investigation is required to verify whether the preferable density dependence is kept in LHD or improvement is specific to pellet injection.

Research in both tokamaks and helical devices<sup>14,15</sup> has demonstrated the presence of neoclassical bootstrap currents. The magnetic field of LHD is excited in a real steady state by using superconducting coils. Therefore, the applied voltage is extremely low and ohmic currents are absolutely excluded. The capability for long-pulse discharges can also eliminate the ambiguity of time dependent behavior. A toroidal current of up to 50 kA has been observed in a discharge with co-injected NBI of 1.5 MW, while the equivalent current to generate the rotational transform in the vacuum magnetic field of LHD is 700 kA at 1.5 T. The rough estimate of the current drive efficiency,  $I_p \bar{n}_e R / P$ , is around  $3 \times 10^{18} \text{ Am}^{-2}/\text{W}$ . Figure 9 shows the temporal behavior of plasma currents including both the Ohkawa currents and bootstrap currents. It takes a few seconds to build up currents, which is the same order of the classical  $L/R$  time. A precise investigation will progress in LHD making full use of these advantages of a long pulse and no toroidal electric field. In all of the NBI discharges, currents flow in the paramagnetic direction, which increases the rotational transform. This observation suggests that the bootstrap current flowing

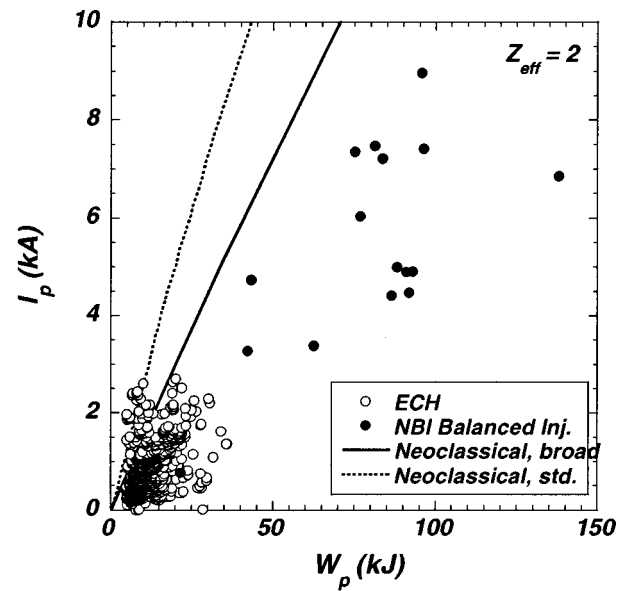


FIG. 10. Observed toroidal currents as a function of the stored energy. Open circles: ECH. Closed circles: Balanced NBI. Prediction from neoclassical theory is also shown. Solid line: Assume broad pressure profile,  $p = p_0(1 - \rho^2)(1 - \rho^8)$ . Dotted line: assume standard pressure profile  $p = p_0(1 - \rho^2)^2$ .

in the paramagnetic direction cancels the currents in the diamagnetic direction driven by counter-injection. In the case of co-injection, currents are enhanced by the sum of the Ohkawa and bootstrap currents. Observed currents with co-injection decrease in the high-density regime, which is explained by the degradation of current-drive efficiency of NBI. Figure 10 indicates that the toroidal currents observed in balanced injection increases in proportion with the stored energy, which reflects the pressure gradient. A neoclassical estimate<sup>16</sup> for bootstrap currents bounds the upper limit of the experimental observation, which is explained by a shortage of pulse length to ramp to the full current.

## V. BOUNDARY PHENOMENA AND CONTROL

Twenty-one dome-type Langmuir probes are set on a divertor plate for investigation of the characteristics of the divertor plasma in LHD. The probe tips are made from molybdenum rods ( $\phi$  2 mm), and the spatial resolution of this probe array is 5–15 mm. The LHD plasma is surrounded by a separatrix with four divertor legs. This probe array can detect two of them. Using this probe array, electron density and temperature of the divertor plasma just in front of the divertor plate and the profiles of the particle flux on the divertor plate are measured. The measurement of the ion saturation current, i.e., particle flux profiles, clearly indicates two peaks. The full width at half maximum is about 10 mm, which is independent of core plasma parameters. These peak positions coincide with the position where the long (a few km) magnetic field lines connect to the divertor plate from the ergodic layer just outside of the last closed flux surface. Typical particle flux is  $1 \times 10^{22} \text{ m}^{-2}/\text{s}$  in NBI plasmas. Elec-

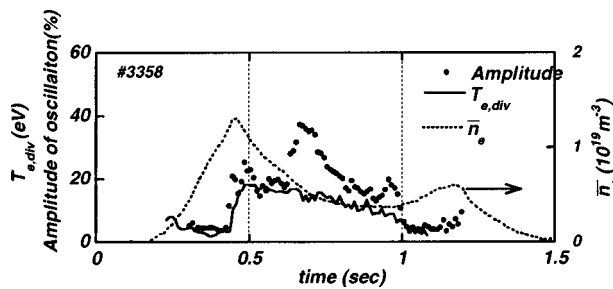


FIG. 11. Probe measurements of divertor plasmas in the discharge shown in Fig. 3(a).

tron temperature and density are measured by the single probe method. The typical values of them are 5–30 eV and  $0.5\text{--}2 \times 10^{18} \text{ cm}^{-3}$ , respectively.

Strong pumping phenomena are frequently observed especially in hydrogen discharges. The density decreases to about half the value even during gas-puff fueling. In the pump-out phase, large oscillations in ion saturation current are observed at the divertor probe array. The amplitude of this oscillation is 20%–60% of the dc component. There is no obvious peak frequency in the power spectrum of this oscillation, but there is a very gently sloping hill in the range of 1–100 kHz. After the beginning of this oscillation, the density starts to decrease. The electron temperature in front of the divertor plate rises up to five times larger than before. Usually, this relatively high temperature is not sustained, and it gradually goes down. The oscillation is terminated when the electron temperature becomes below 10 eV in divertor plasma. The pumping phase is also terminated at this time, and the density starts to increase again (see Fig. 11). The electron temperature of the surrounding plasma appears to be a key parameter for the pumping mechanism.

While hydrogen discharges are accompanied by the density pump-out, a low recycling condition has been realized, which has been strongly related to confinement improvements.<sup>17</sup> The temperatures of both electrons and ions has reached 200 eV at the outermost flux surface and the density sharply drops to zero at the outside of the last closed flux surface. Although a clear confinement improvement has not been observed yet, the above mentioned characteristics for density and temperature have not been observed in helical devices to date and an increase of edge temperatures would be expected with increased input power in further experiments, which is a key of confinement improvement.

A local island divertor (LID) experiment was performed using the LID magnetic configuration, where an  $m/n = 1/1$  island is generated by 20 perturbation coils, to study the effect of the LID configuration on the ECH plasma. In this experiment, the outward heat and particle fluxes cross the island separatrix and flow along the field lines to the back side of the island, where target plates would be placed as a divertor head.<sup>18,19</sup> The particles recycled there are pumped, and hence, the geometrical shapes of the divertor head and pumping duct will be designed to form a closed divertor configuration with a high pumping efficiency. The divertor head was, however, not used in the first campaign. It is found that the plasma parameters change significantly with the LID

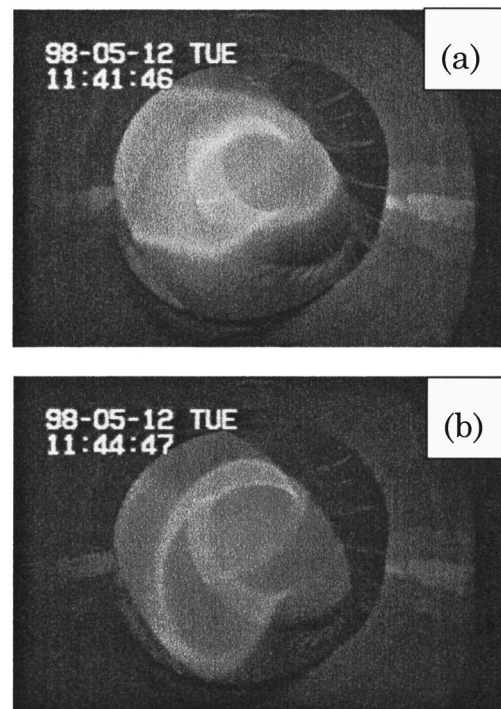


FIG. 12. Tangential views of ECH plasmas. (a) Without LID magnetic field. (b) With LID magnetic field.

configuration when the plasma is not fully expanded in the standard LHD configuration, as shown in Fig. 12(a). In this case, the plasma becomes expanded well in the LID configuration, as shown in Fig. 12(b). Temporal evolution of the stored energy, the density, the radiation power, and the OV and CIII radiation intensities are shown in Fig. 13, where a comparison between discharges in the LID configuration and in the standard LHD configuration is made at fixed levels of the ECH power and gas puffing. The radiation power measured with a bolometer and the OV and CIII radiation intensities decrease significantly with the LID configuration, as

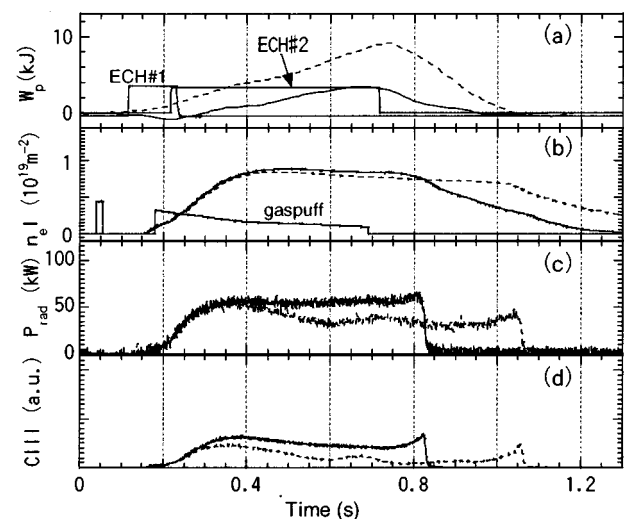


FIG. 13. Temporal behavior of ECH plasmas shown by TV pictures in Fig. 12. Solid lines: Without LID magnetic field. Broken lines: With LID magnetic field.



shown in Figs. 13(c) and 13(d), while the density decreases a little. The stored energy increases in the LID configuration, suggesting improved confinement. However, since the plasma radius expands in the LID configuration, compared with that in the standard LHD configuration, the obtained energy confinement time is not improved significantly at this stage of the experiment, but is consistent with the ISS95 scaling law.

## VI. DISCUSSIONS AND SUMMARY

The experiments on LHD have started on 31 March 1998, after an eight-year construction period, which expands confinement studies on currentless plasmas to a large scaled machine. Physics experiments on currentless toroidal plasmas are progressing based on the technical achievements during the construction phase. Plasma performance has been rapidly improving. Heating by 3 MW of NBI has provided plasmas with a fusion triple product of  $8 \times 10^{18}$  keV m<sup>-3</sup> s at a magnetic field of 1.5 T. An electron temperature of 1.5 keV and an ion temperature of 1.4 keV have been achieved. A study of confinement of NBI heated plasmas has shown a trend similar to the prior scaling laws, however, a significant improvement compared with the ISS95 expression by a factor of 1.5 and comparable confinement to the Lackner-Gottardi scaling have been obtained. In the present experimental condition, the absorbed power of NBI depends on the operational density. Therefore, it needs careful attention and further systematic scans to separate the power degradation from a favorable density dependence. The operational density limit as well as the confinement improvement with increased density have been changing drastically along with the progress of wall conditioning. In this stage, these enhancements cannot be explained by a simple dependence on power density and  $Z_{eff}$ . Therefore, a conclusion awaits for well-conditioned experiments in the near future.

Fueling of particles is reconfirmed as an important experimental technique for large-scale helical systems. An escape of particles from the core of the plasma has been highlighted in hydrogen discharges. Low recycling conditions are achieved simultaneously, which leads to high temperatures at the edge. This observation is explained from the concept of the high-temperature divertor.<sup>17</sup> Combination with central fueling by pellet injection has mitigated a hollow density profile temporarily. Helium discharges facilitate density control through high recycling. Here it should be noted that the high edge temperature is not specific to hydrogen discharges. A careful control of helium gas puffing can realize a similar high edge temperature.

The knowledge of transport, MHD, divertor, and long-pulse operation is now rapidly increasing, which means the successful progress of physics experiments. Interesting and important phenomena related with these issues have already been found. The advantage of the superconducting device is becoming clearer especially when the steady-state experiments are pursued.

## ACKNOWLEDGMENTS

The authors are grateful to all collaborations with universities and other institutes. Efforts by the industrial companies to complete the LHD construction are greatly appreciated. The authors express their deepest gratitude posthumously to J. Yamamoto and H. Kaneko for their great contribution to the LHD project. Correction of the manuscript by Dr. L. R. Baylor is acknowledged.

- <sup>1</sup>O. Motojima, N. Yanagi, S. Imagawa, *et al.*, *Proceedings, 16th International Conference on Fusion Energy, Montreal, 1996* (International Atomic Energy Agency, Vienna, 1997), Vol. 3, p. 437.
- <sup>2</sup>M. Fujiwara, K. Yamazaki, M. Okamoto, *et al.*, *J. Fusion Energy* **15**, 7 (1996).
- <sup>3</sup>A. Iiyoshi, *Proceedings, 16th International Conference on Fusion Energy, Montreal, 1996* (International Atomic Energy Agency, Vienna, 1997), Vol. 1, p. 113.
- <sup>4</sup>K. Toi, S. Okamura, H. Iguchi, *et al.*, *Proceedings, 14th International Conference on Plasma Physics and Controlled Nuclear, Würzburg, 1992* (International Atomic Energy Agency, Vienna, 1993), Vol. 2, p. 461.
- <sup>5</sup>V. Erckmann, F. Wagner, J. Baldzuhn, *et al.*, *Phys. Rev. Lett.* **70**, 2086 (1993).
- <sup>6</sup>K. Ida, K. Kondo, K. Nagasaki, *et al.*, *Phys. Rev. Lett.* **76**, 1268 (1996).
- <sup>7</sup>H. Maassberg, C. D. Beidler, and E. E. Simmet, *J. Plasma Fusion Res.* **1**, 230 (1998).
- <sup>8</sup>H. Idei, K. Ida, H. Sanuki, *et al.*, *Phys. Plasmas* **1**, 3400 (1994).
- <sup>9</sup>S. Murakami, N. Nakajima, and M. Okamoto, *Trans. Fusion Tech.* **27**, 256 (1995).
- <sup>10</sup>S. Sudo, Y. Takeiri, H. Zushi, F. Sano, K. Itoh, K. Kondo, and A. Iiyoshi, *Nucl. Fusion* **30**, 11 (1990).
- <sup>11</sup>K. Lackner and N. A. O. Gottardi, *Nucl. Fusion* **30**, 767 (1990).
- <sup>12</sup>M. Murakami, T. S. Bigelow, J. B. Wilgen, *et al.*, *Proceedings, 14th International Conference on Plasma Physics and Controlled Nuclear, Würzburg, 1992* (International Atomic Energy Agency, Vienna, 1993), Vol. 2, p. 391.
- <sup>13</sup>U. Stroth, M. Murakami, H. Yamada, F. Sano, R. A. Dory, S. Okamura, and T. Ohbiki, *Nucl. Fusion* **36**, 1063 (1996).
- <sup>14</sup>M. Murakami, B. A. Carreras, L. R. Baylor, *et al.*, *Phys. Rev. Lett.* **66**, 707 (1991).
- <sup>15</sup>H. Yamada, S. Kubo, K. Watanabe, *et al.*, *Nucl. Fusion* **34**, 641 (1994).
- <sup>16</sup>K. Y. Watanabe, N. Nakajima, M. Okamoto, K. Yamazaki, Y. Nakamura, and M. Wakatani, *Nucl. Fusion* **35**, 335 (1995).
- <sup>17</sup>N. Ohyabu, T. Watanabe, H. Ji, *et al.*, *Nucl. Fusion* **34**, 387 (1994).
- <sup>18</sup>A. Komori, N. Ohyabu, T. Watanabe, *et al.*, *Proceedings, 15th International Conference on Plasma Physics and Controlled Nuclear, Seville, 1994* (International Atomic Energy Agency, Vienna, 1995), Vol. 2, p. 773.
- <sup>19</sup>A. Komori, N. Ohyabu, S. Masuzaki, *et al.*, *Proceedings, 16th International Conference on Fusion Energy, Montreal, 1996* (International Atomic Energy Agency, Vienna, 1997), Vol. 2, p. 3.